

Observations of the Crab Nebula with MACE (Major Atmospheric Cherenkov Experiment)

Borwankar C.^{a,*}, Sharma M.^{a,*}, Hariharan J.^a, Venugopal K.^a, Godambe S.^a, Mankuzhyil N.^a, Chandra P.^{a,*}, Khurana M.^{a,b}, Pathania A.^a, Chouhan N.^a, Dhar V. K.^{a,b}, Thubstan R.^a, Norlha S.^a, Keshavanand^a, Sarkar D.^{a,b}, Dar Z. A.^a, Kotwal S. V.^a, Godiyal S.^a, Kushwaha C. P.^a, Singh K. K.^{a,b}, Das M. P.^a, Tolamati A.^{a,b}, Ghosal B.^{a,b}, Chanchalani K.^a, Pandey P.^a, Bhatt N.^a, Bhattcharyya S.^{a,b}, Sahayanathan S.^{a,b}, Koul M. K.^a, Dorjey P.^c, Dorji N.^c, Chitnis V. R.^c, Tickoo A. K.^{a,1}, Rannot R. C.^{a,b}, Yadav K. K.^{a,b}

^a*Astrophysical Sciences Division, Bhabha Atomic Research Centre, Mumbai 400085, India.*

^b*Homi Bhabha National Institute, Mumbai 400094, India.*

^c*Department of High Energy Physics, Tata Institute of Fundamental Research, Mumbai, India.*

Abstract

The Major Atmospheric Cherenkov Experiment (MACE) is a large size (21m) Imaging Atmospheric Cherenkov Telescope (IACT) installed at an altitude of 4270m above sea level at Hanle, Ladakh in northern India. Here we report the detection of Very High Energy (VHE) γ -ray emission from Crab Nebula above 80 GeV. We analysed ~ 15 hours of data collected at low zenith angle between November 2022 and February 2023. The energy spectrum is well described by a log-parabola function with a flux of $\sim (3.46 \pm 0.26_{stat}) \times 10^{-10} \text{ TeV}^{-1} \text{ cm}^{-2} \text{ s}^{-1}$, at 400 GeV with spectral index of $2.09 \pm 0.06_{stat}$ and a curvature parameter of $0.08 \pm 0.07_{stat}$. The γ -rays are detected in an energy range spanning from 80 GeV to ~ 5 TeV. The energy resolution improves from $\sim 34\%$ at an analysis energy threshold of 80 GeV to $\sim 21\%$ above 1 TeV. The daily light curve and the spectral energy distribution obtained for the Crab Nebula is in agreement with previous measurements, considering statistical and systematic uncertainties.

Keywords: gamma rays: general – telescopes – techniques: miscellaneous – methods: data analysis – individual: Crab Nebula

1. Introduction

The Crab Nebula, a supernova remnant (SNR), located at a distance of ~ 2 kpc [1], was detected in 1054 A.D. [2, 3]. It remains one of the most widely studied astrophysical sources across various wavelengths of electromagnetic spectrum [4, 5, 6, 7, 8, 9, 10, 11, 12, 13, 14]. Observations of emission from the nebula region at every accessible wavelength have resulted in a well-determined broadband spectral energy distribution (SED) of the Crab Nebula.

In a widely accepted classical model of the Crab Nebula, it consists of a pulsar at its center, a shocked pulsar wind nebula, a bright expanding shell of thermal gas or thermal filament, and a faint freely expanding supernova remnant located outside the edge of nebula [15, 16].

The pulsar injects energy in the form of a magnetized, cold, and ultra-relativistic wind of electron-positron pairs at a constant rate into the nebula region. The randomized electron-positron pairs produce synchrotron radiation from radio to high energy (HE) γ -rays of few 100 MeV. The upscattering of low energy photons by the relativistic electron-positron pairs via inverse Compton (IC) process leads to the emission of very high energy (VHE) γ -ray photons in the range from few GeV to 100 TeV from the Crab nebula [17, 18, 19]. These underlying radiative processes predict time-independent luminosity of the source over a timescale of few hundred years [20]. However, several rapid and bright flares of different magnitudes have been observed from the Crab Nebula since 2009 by the space-based γ -ray detectors in the HE γ -ray band [21, 22, 23, 24, 25, 26]. The measured enhancements in HE fluxes up to few GeV are attributed to the synchrotron component of the nebula emission while VHE fluxes from the IC component have shown no significant changes and

*Corresponding author

Email addresses: chinmay@barc.gov.in (Borwankar C.),
mradul@barc.gov.in (Sharma M.), chandrap@barc.gov.in
(Chandra P.)

¹Deceased

remain consistent with the average emission level [27, 28]. Thus, Crab Nebula remains a constant and steady emitter of VHE photons and has been used as a standard candle [29] in the field of ground-based gamma-ray astronomy for more than three decades. It is also used for cross-calibration of telescopes, monitoring of the instrument response over time, and expressing the emission level of other astrophysical sources in the Crab Unit (C.U.) in observational astronomy.

The development of Imaging Atmospheric Cherenkov Telescopes (IACTs) for ground-based VHE astronomy has unveiled the γ -ray sky in an unprecedented way. Today, more than 270² sources of GeV-TeV γ -rays have been discovered in the known universe over a short time span with IACTs being a major actor in the field [30, 31, 32]. With the aim of detecting γ -rays of energies down to ~ 30 GeV with high point source sensitivity, a state-of-the-art IACT, MACE (Major Atmospheric Cherenkov Experiment) setup at Hanle, Ladakh in northern India, has been carrying out regular observations of Crab Nebula since September 2021. In this paper, we present the first light results from Crab Nebula using MACE observations conducted between November 2022 to February 2023, totalling ~ 15 hours of observation time. We estimate the differential energy spectrum of Crab Nebula in the zenith angle range of 10° to 35° . The analysis covers both the ON source and the OFF source region during the observation period.

This paper is organized as follows: Section 2 provides an introduction to MACE. Section 3 details about the Monte Carlo (MC) simulations carried out for MACE. Section 4 covers the Observations and Data analysis practices employed in handling the simulation and observation data. The validation of the MC simulations by comparison with the observed data is discussed in Section 5. The performance of MACE telescope is evaluated by estimating various parameters like Energy threshold, Energy and angular resolution and integral flux sensitivity in Section 6. Finally we conclude by discussing the results obtained and conclusion in Section 7.

2. The MACE Telescope

MACE is the latest major step in the long-development of ground-based VHE gamma-ray astronomy program in India [33]. It indirectly detects VHE γ -ray photons emitted from the galactic or extragalactic sources by collecting

the Cherenkov light produced by the cascade of relativistic charge particles in an extensive air shower, initiated by the interaction of GeV-TeV γ -rays, within the Earth-atmosphere [34]. MACE is located at Hanle ($32^\circ 46' 46''$ N, $78^\circ 58' 35''$ E) in the Himalayan ranges of North India [35, 36, 37]. Located at an altitude of 4270m above sea level, it stands as the only operational IACT such a high altitude. The telescope has a 21m diameter quasi-parabolic reflector with an f-ratio of 1.2 and a focal length of 25m. Its light collector consists of 356 mirror panels, each measuring $984 \text{ mm} \times 984 \text{ mm}$. Each panel is composed of four $488 \text{ mm} \times 488 \text{ mm}$ facets of spherical mirrors made of aluminum with SiO_2 coating. The total light collector area amounts to $\sim 337 \text{ m}^2$.

The mirror facets have a graded focal length ranging from 25-26.52m [38]. The graded focal length ensures that the on-axis spot size is minimum at the focal plane. The MACE employs the Active Mirror Control system to align individual mirrors panels through computer-controlled actuators to ensure optimal focusing at all zenith angles. The MACE camera [39] is equipped with 1088 photomultiplier tubes (PMTs). The entire camera is segmented into 68 sections, referred to as Camera Integrated Modules (CIM). Each CIM consists of 16 PMTs with a uniform pixel resolution of 0.125° and fitted with a Compound Parabolic Concentrator (CPC) featuring a hexagonal aperture of size 0.125° and a circular exit that matches the active photo-collection area of the PMT. CPCs eliminate the dead space between PMTs. Out of a total of 68 CIMs, the innermost 36 CIMs consisting of 576 PMTs are utilized for MACE trigger generation. The field of the view for the total trigger region measures $\sim 2.62^\circ \times 3.02^\circ$ whereas the optical field of view of MACE camera is $\sim 4.36^\circ \times 4.03^\circ$. The MACE camera layout with 3, 4 and 5 CCNN trigger patterns is shown in Figure 1.

3. Monte Carlo simulations

One of the main challenges in the IACT data analysis arises from the absence of calibrated sources of TeV γ -rays. Monte Carlo simulations offers a solution by simulating the expected Cherenkov radiation produced from γ -rays and cosmic rays induced showers and modelling the response of an IACT to this light. A comprehensive database of simulated images of γ and hadron-induced air showers provides a necessary calibration to reconstruct particle type, energy, and arrival direction of the events detected by an IACT. This includes the development of Machine Learning (ML)

²<http://tevcat2.uchicago.edu/>

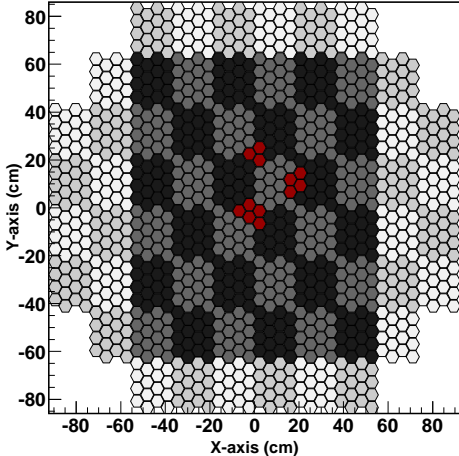


Figure 1: The MACE camera configuration consists of 1088 pixels organized into 68 modules, each containing 16 PMTs (photo-multiplier tubes) [36]. The trigger signal originates from a darker shaded region encompassing 576 pixels. The typical trigger patterns for different programmable schemes (3, 4, 5 CNNN :-Close Cluster Nearest Neighbor) are depicted in red. The trigger configuration of 4 (CCNN) pixels is implemented in MACE.

models for estimating the type and energy of the events, as well as calculation of instrument response functions of the telescope.

The development of γ and cosmic ray induced air showers through the atmosphere and the production of Cherenkov light were simulated using CORSIKA v6.990 [40]. The atmospheric density profile and extinction coefficients for visible light are estimated using U.S. standard atmospheric model. We use the IACT-Bernlohr routines [41] from CORSIKA to model the propagation and absorption of Cherenkov radiation through the atmosphere up to the ground level. These routines provide data about the position, orientation, wavelength, time of arrival and number of Cherenkov photons emitted during EAS development. The Cherenkov photons which intersect with the fiducial sphere of the size equal to telescope radius located at telescope position are stored.

We simulated a total of 24.8×10^6 γ -ray induced showers and 4.96×10^8 proton induced air showers respectively. The γ -ray showers were divided into three independent

	γ		Proton	
	All	Triggered	All	Triggered
Training	8.9×10^6	60000	3.96×10^8	60000
Validation	2.5×10^6	15000	1.0×10^8	15000
Response	13.4×10^6	90000	-	-

Table 1: Number of events used for training validation and estimation of telescope response functions

samples with sizes of 8.9×10^6 , 2.5×10^6 and 13.4×10^6 events respectively. These samples are used for training random forest models for classification and regression, for validation of trained random forest models and for estimation of various telescope response matrices respectively. We estimate background rates in MACE data using dedicated OFF runs (see section 4) and hence we do not require evaluation of response matrices for cosmic rays. The simulated proton induced air showers were thus divided into 2 independent samples consisting of 3.96×10^8 and 1×10^8 events used for random forest training and validation. A small set of Helium induced air showers consisting of few million showers in the zenith range of $15^\circ - 25^\circ$ is also generated using CORSIKA. The Helium showers are used only for the comparison of observed event rates with integral rates estimated from the simulations(see section 5). The number of events used for training, validation and generation of response matrices are summarised in Table 1

The γ -rays were simulated with a differential energy spectrum given by $dN/dE \propto E^{-2.59}$ in the energy range of 10 GeV to 20 TeV whereas the cosmic ray protons were simulated in the energy range of 20 GeV to 20 TeV with a spectral index of 2.7. All the showers were generated for zenith angles ranging from 10° to 35° in increments of 1° , to cover the zenith range of Crab data analysed in this work. The azimuth dependence of extensive air showers was incorporated by simulating showers at azimuth angles ranging from 0° to 315° in increments of 45° for each zenith. To accelerate simulations and address low global trigger efficiency, each generated shower was utilized 10 times, with the telescope placed at 10 randomized locations within a 650 m circle around the shower axis. The protons were simulated with their arrival direction within 3° of the telescope pointing direction. The Crab nebula being the point source for IACTs, we keep arrival direction of all simulated γ -rays along the telescope pointing direction.

The quantum efficiency of MACE PMTs and reflec-

tivity of the MACE mirrors is accounted for by using the CEFFIC option of the Bernlohr routines. The wavelength dependence of quantum efficiency and reflectivity of MACE telescope is reported in [42]. We developed a C++/ROOT based program to simulate the response of MACE [43] to air showers. The program simulates the reflector, the camera geometry and the camera electronics. While specular reflection is used to ray trace individual Cherenkov photons from the mirror surfaces, the finite optical Point Spread Function (PSF) of the reflector is simulated using Gaussian smearing of reflected direction. The smearing angle is set to a value such that the simulated optical PSF matches with the optical PSF measured during mirror alignment observations performed on the pole star. Single photo-electron pulses are added to each PMT with an average rate of 293 MHz to account for the contribution from light of night sky (LONS). The rate of LONS induced photo-electrons is estimated from the observations reported by nearby Himalayan Chandra Telescope (HCT) [44, 42]. The detailed simulations of various parts of camera electronics related to trigger and data acquisition are performed and shower images which pass preset trigger criterion are stored in ROOT files. To realistically simulate the electronics the PMT pulses are modeled by superposition of the single photo-electron pulses, where each single photo-electron pulse is approximated by a Gaussian shape. The amplitude of the single photo-electron pulse is set on the basis of lab-measured gain of reference PMTs. The MACE event trigger is generated through two level trigger system, where a first level trigger checks the coincidence of threshold crossing pulses within a module of 16 pixels (see Figure 1). The second level trigger detects the events which are spread over pixels located in 2 or more than 2 neighbouring modules. The coincidence gate width of first level trigger is 5 ns, where as it is 10 ns for second level. The MACE simulation program implements the two level trigger system including the pulse shaping at outputs of PMT pulse discriminators, time coincidence of output square pulses generated by each PMT as well as first level trigger (FLT) modules. The amplification of PMT pulses by low and high gain channels, digitisation of PMT pulses by DRS4 12 bit- analog to digital converter (ADC) assembly, various jitters in trigger and data acquisition are simulated to generate the output images in a format equivalent to the real MACE data. The output images in simulations thus consist of 2 arrays with length equal to number of PMTs, consisting data of of integrated

digital counts for high and low gain pathways. The output images also have pulse profile data and information on ADC saturation status for high and low gain paths. The complete analysis chain described in Section 4 is then applied on the simulated images.

The telescope response simulation, used to estimate various performance parameters as described in earlier studies [36, 37] did not include the camera electronics such as trigger and data acquisition system. The old trigger simulation consisted of a topological trigger where single channel discrimination threshold was simulated in terms of number of photo-electrons collected at a PMT. The simulated image consisted of an array of number of photo-electrons collected at each PMT. All machine learning models and instrument response functions used in the analysis of Crab Nebula observations have been generated using the new simulation program that includes simulation of complete electronics chain.

The Crab field of view contains 3 bright stars namely, ζ -Tauri (Mag 2.91), ω -Tauri (Mag 4.81) and 121-Tauri (Mag 5.34) at an angular distance of 1.2° , 1.5° and 1.7° from the center of FoV of Crab, respectively. During the Crab observation runs, MACE PMTs were operated at a low gain of ~ 24000 , corresponding to an average single photo-electron pulse height of 8 mV . However, the presence of bright stars and high average ambient LONS in galactic plane, disabled some PMTs due to high anode current and trigger masking of some channels occurred near the position of the bright stars. To minimize the number of disabled and trigger masked pixels, we operated MACE with a high discrimination threshold of 90 mV during Crab observations. The operational configuration corresponds to single channel discrimination threshold of ~ 11 photo-electrons with a 4 close cluster near neighbor trigger (CCNN). The details about the working of CCNN is available in our previous work [36].

4. Observations and Data Analysis

Observations of Crab Nebula were carried out using MACE at various zenith angles between November 2022 to February 2023. We have evaluated the performance of the telescope at zenith angles ranging from 10° - 35° . The data were collected in the ON/OFF mode for $\sim 15/12$ hours respectively. The OFF sky region, devoid of any known γ -ray source, was observed within the same zenith range as that of ON source to collect the OFF source data.

After applying the Good Time Interval (GTI) (refer Section 4.1), we obtained a total of 12.57 hours and 8.32 hours of ON and OFF source data respectively.

4.1. Data Quality Monitoring

The MACE console serves as a central control unit where the system configuration parameters and operation sequences are selected. Central Camera Control (CCC) collects the telemetry data from all the CIMs and sends it to the Property Server (PS) for data storage. Two types of telemetry parameters are recorded based on their impact on the system performance: the "Critical Parameters" like Anode Current (AC), Single Channel Rate (SCR), System PCR (Prompt Coincidence Rate) and Module CCR (Chance Coincidence Rate), logged every second, and the "Routine Parameters" like High Voltage (HV), Discriminator Threshold (D_{th}), power supply Status and Temperature, logged every minute. In-house developed ROOT-based software is used to analyse the Critical and the Routine telemetry data to carry out the data quality checks for proper hardware functioning of MACE camera. Analysis of telemetry data ensure that the hardware is operating within the acceptable ranges.

To prepare the science data for the event analysis, a utility called GTI was developed. This utility checks the variation of the critical and the routine telemetry parameters and selects time intervals where telemetry parameters remains within the acceptable range. This utility is implemented in three stages: Global GTI, which deals with parameters for the entire camera, module GTI, which deals with module-based parameters and channel GTI, which deals with individual channel parameters. GTI on the telemetry data generates good time intervals for the Critical and the Routine parameters, combining them to form a single GTI for a particular run.

4.2. Calibration & Trigger

The event data (ON data) contains low-gain and high-gain charges from all 1088 PMTs. High-gain channels utilize an additional amplifier (with a gain of 10) compared to that of low-gain channels to accommodate even the weaker Cherenkov pulses. The charges are calculated from the 24 samples from the Domino Ring Sampler (DRS) version 4 [45] operating at rate of 1 GS/s. To reduce the data volume, the charges are calculated in the camera itself. Pulse profiles of 31 ns are stored only for the channels above a particular threshold. In addition to the charge and profile, the dataset includes hardware information and flags to

ensure data reliability. The Cherenkov, sky, and calibration data along with the timing information are stored in the same file with corresponding flags. The trigger rate of MACE follows zenith angle dependence of the form $R(\theta) \sim R_0(\theta)\cos^m(\theta)$, where θ is the zenith angle of observation and $m = 0.41$. Observations with rates deviating more than 10% with respect to a value estimated from above relation were discarded from the dataset. We also discarded data affected by technical problems or poor sky conditions. The sky conditions are assessed based on data from the on-site sky monitoring system as well as the fluctuations in single channel rates. The MACE employs an altitude-azimuth mount with a 27 m diameter circular track that can provide the tracking accuracy of better than 1 arc-minute under wind speeds of up to 30 km h^{-1} . The pointing of the telescope is verified for each source by observing an optical star having similar declination as that of γ -ray source. The telescope also incorporates an active mirror alignment control system to correct for any deformations due to gravity. The exact location of the star was compared with the reconstructed positions of the star in the camera after the pointing run. The final telescope mis-pointing was corrected offline during the pre and post-transit phase of Crab Nebula. The pointing accuracy was measured to be better than 1 arc-minute. The MACE records 1000 calibration and 1000 sky pedestal events after every 300 seconds of collecting Cherenkov data. The LED calibration events are used to estimate relative gain factors of channels and to 'flat-field' images. The mean value and variance of the night sky background for each channel are estimated from sky pedestal events. After calibration, single bad channels (a specific channel that is malfunctioning or inactive. This can be due to various issues such as a dead pixel, high or low anode current, or other related problems.) that are part of the images are assigned values obtained from the interpolation of neighboring channels.

4.3. Image cleaning and reconstruction

The night sky background (NSB) plays a significant role in modulating the performance of MACE. This background is commonly referred to as the light of the night sky (LONS). During the moonless nights, the night sky background consists of the diffuse light contributed by the ambient sources such as the surroundings, starlight, and zodiacal light. The measurement of the LONS at the nearby Himalayan Chandra Telescope (HCT) has been carried out [44]. The intensity of the NSB in the wavelength

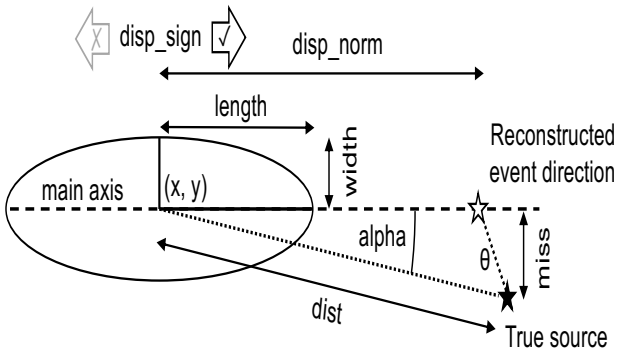


Figure 2: Illustration of few Hillas parameters of a typical Cherenkov image [48].

range 240-650 nm is estimated to be $\sim 2.6 \times 10^{12}$ photons $\text{m}^{-2}\text{s}^{-1}\text{sr}^{-1}$ [35]. To improve the quality of the Cherenkov light triggered images, a two-stage image cleaning procedure is employed using the standard cleaning method [46]. In the first stage, a core set of image pixels are identified where the total charge within the image exceeds a given threshold. The second stage involves identifying the boundary pixels where total charge is more than a given threshold. Standard tail-cut cleaning is applied to every image where each pixel with Signal to Noise ratio (S/N) of ≥ 6.5 are retained as picture pixels while the boundary pixels are selected if they have S/N ratio of ≥ 2.65 and are adjacent to atleast one picture pixel. The isolated pixels are retained only if their S/N ratio is ≥ 10.0 . while the remaining pixels are excluded from further analysis.

Once the images are cleaned they are characterised by calculating the Hillas parameters [47]. These parameters are based on the zeroth, first and second moments of images weighed by charge content of the pixels. Some of the Hillas parameters used in this work as inputs to the random forest models for event classification, direction reconstruction and energy prediction are depicted in the Figure 2. Additionally, we have used Leakage parameter (ratio between the light content in the camera two outer most pixels to the total light content) to quantify the extent of image truncation.

4.4. Event Classification

The γ and hadron events are distinguished by carefully analyzing the spatial distribution of Cherenkov photons on the image plane of the camera. Only a very small fraction ($\sim 10^{-5}$) of γ -ray events constitute the signal compared to the background generated by cosmic rays. Furthermore,

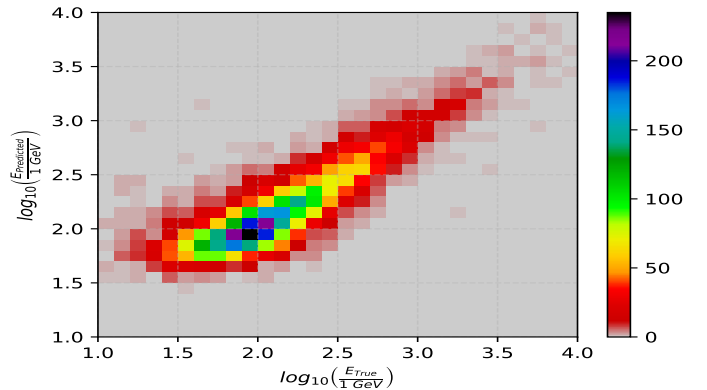


Figure 3: Distribution of simulated γ ray events in True versus the estimated energy using the Random Forest method. The color of the bin represents the number of γ -ray events.

the segregation of γ -ray events from the background is complicated by the NSB triggered images, which can obscure the signal of interest. We use multivariate techniques for the discrimination of γ -rays and hadrons employing multiple variables to analyze the data and identify patterns that distinguish γ -rays from hadrons. The Random Forest method (RFM) [49] is employed for γ -hadron classification. The events are classified using a single classification parameter, known as the *hadronness*. The Hillas parameters like Length, Width, Distance, Size, Frac2 (ratio of the sum of two highest pixel signal to the sum of all the pixel signal), and Leakage are used for training the Random Forest classifier employing scikit-learn [50]. The values of *hadronness* range between 0 and 1 with higher indicating that the classified event is more like a hadron event. The value of *hadronness* is chosen to maximize the significance of signal detection. In this work, we have applied a cut value of $\text{Hadronness} \leq 0.14$ to categorize the image as a γ -ray-like event.

4.5. Energy reconstruction

The energy of γ -rays is reconstructed using the regressive RFM. The RFM was trained using standard Hillas parameters (Size, Distance, zenith, Leakage) and a simulated dataset consisting of 160,000 γ -rays, as described in the simulation section. Figure 3 displays the estimated energy as a function of the true energy illustrating that the reconstructed γ -ray energy closely aligns with the true γ -ray energies.

With the RFM, we have estimated the relative importance [51] of all the training parameters (features) used

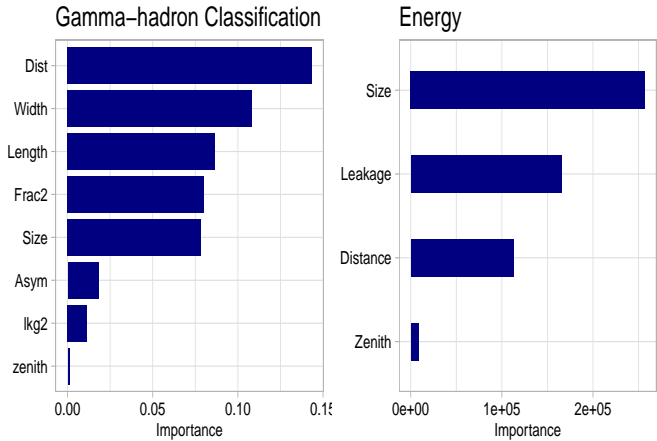


Figure 4: Relative importance of various parameters for gamma-hadron classification (Left panel) and energy reconstruction (Right panel).

in classification and the energy estimation employing the simulated gamma and proton events. The relative importance is determined by calculating the mean decrease in accuracy, which measures the model performance without that specific variable. A higher value indicates a greater importance of that variable in prediction. The left panel of Figure 4 illustrates the relative importance of various parameters in classification. The relative importance of various parameters in energy estimation is shown in the right panel of Figure 4.

5. Validation of the MC simulation by comparisons with observation data

The MC chain was validated at 3 stages of analysis. This includes comparison of experimental event rates with simulated background rates and comparison of experimental Hillas parameters distributions of background and excess data with simulated background and γ -ray data.

5.1. Rate Comparison

As a first step of validation of MC against the data, we compare the integral event rates above a given size for the data and the MC samples. The event rates of an IACT are dominated by proton and Helium induced air showers. While the protons contribute nearly 80% of the total collected shower images, Helium induced showers produce rest of the events. Figure 5 shows the integral rates due to Protons (red open circles), Helium (green open circles) and their total (magenta open circles) as estimated by MC simulations. The grey dashed line and corresponding open

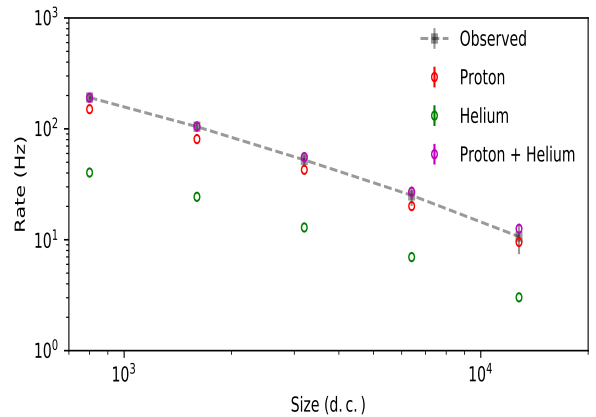


Figure 5: Integral rate of background events above a given size for data (dashed line) and MC. The contribution of proton in the total rate is shown with red open circles, green open circles show contribution of Helium while magenta open circles show total simulated rates.

squares show the variation of observed integral rates as a function of size threshold. We see that, there is a good agreement between simulations and data. We mark here that, although calibrated values of PMT gain, optical PSF and other electronics parameters have been incorporated in the simulations, uncertainties due to variations in atmospheric and sky conditions, degradation of mirrors or their dust deposition can not be measured. Hence an additional parameter of optical efficiency, also termed as telescope gain, is introduced in the simulations for fine tuning. We find that the integral rates estimated by MC simulations match well with the OFF data rates at the optical efficiency value of 1.05.

5.2. Hillas Parameters : Data vs MC

In order to validate the performance of MACE, a comparison of Hillas parameters for background events and the predicted γ -ray-like events observed by MACE telescope $Crab_{OFF/ON}$ observations and those obtained from MC simulations is carried out. A representative comparison of the various image parameters like Length, Width, Distance, Size, Frac2 and Leakage is shown in Figure 6, 7. We find acceptable agreement between the simulated and the observed parameters. However, there is a visible deviation between simulated and observed distributions of Size and Distance parameters at higher values.

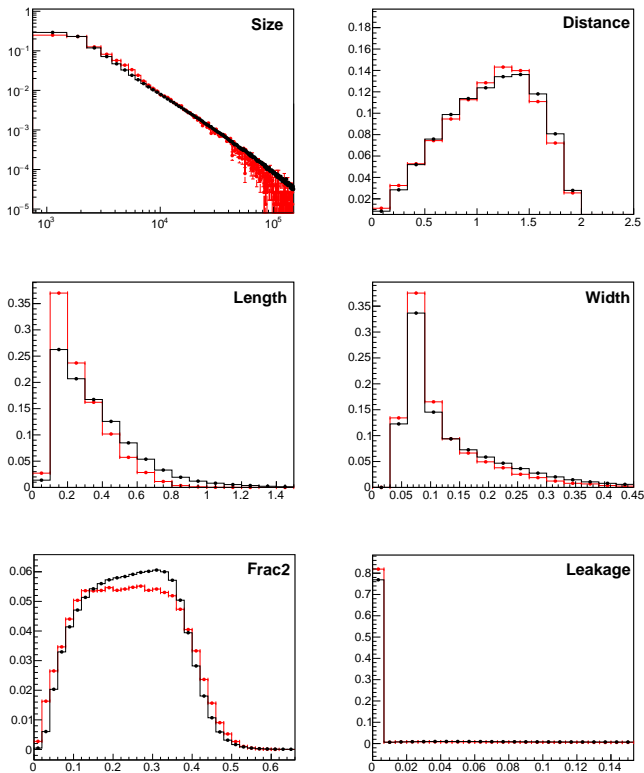


Figure 6: Distribution of various Hillas parameters for the proton events. The black and red lines show the simulation and the observed data points respectively for Size, Distance, Length, Width, Frac2 and Leakage.

6. MACE telescope performance

The performance evaluation of MACE utilized the MC simulations and employed four metrics: energy threshold, energy resolution, angular resolution, and integral sensitivity. The evaluation was carried out using the Random Forest multivariate machine learning method. We mark that we assume power law spectral shape for the Crab nebula with index of 2.6, during the estimation of energy threshold and integral sensitivity.

6.1. Energy Threshold

The threshold energy of a telescope is determined by constructing a differential rate plot of γ -rays utilizing the Monte Carlo simulations as a function of energy. The energy at which this rate plot peaks, signifies the energy threshold (E_{th}) of the telescope. Figure 8 displays the trigger rate plot, modelled by a power law, as a function of true γ -ray energy before and after the analysis cuts in the zenith angle range 10° - 20° , 20° - 30° and 30° - 35° . The

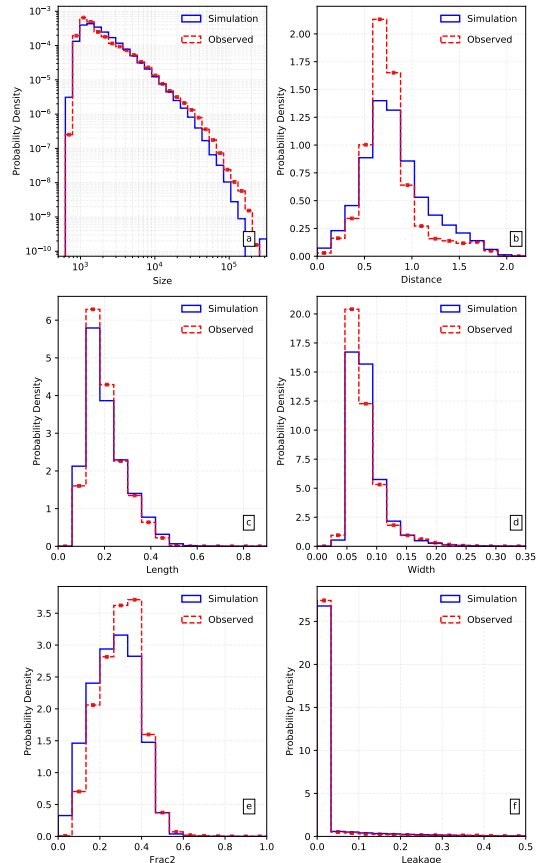


Figure 7: Distribution of various Hillas parameters for the γ -ray excess events extracted by using the RFM and Monte Carlo simulated γ -rays. The solid lines (blue) and the dashed line (red) show the simulation and the observed data points respectively for Size, Distance, Length, Width, Frac2 and Leakage.

γ -ray rate plot shows a broad peak, indicating an energy threshold of ~ 80 GeV. Because the peak of γ -ray rate is relatively broad and extends significantly towards the lower energies, it remains possible to have events below the energy threshold of the telescope. However, below 80 GeV, there is a reduction in the effective area of the telescope (Figure 14), making it challenging to analyze faint sources within this energy range.

6.2. Energy Resolution

The inherent fluctuations in the extensive air shower generation process, as well as the effects of the atmosphere and Earth's magnetic field, have an impact on an IACT's capability to accurately reconstruct the energy of primary γ -rays. These disturbances can modify the physical characteristics of the shower, potentially leading to a spread in the signals, and consequently introducing a bias in the reconstructed energy of the γ -rays. The energy

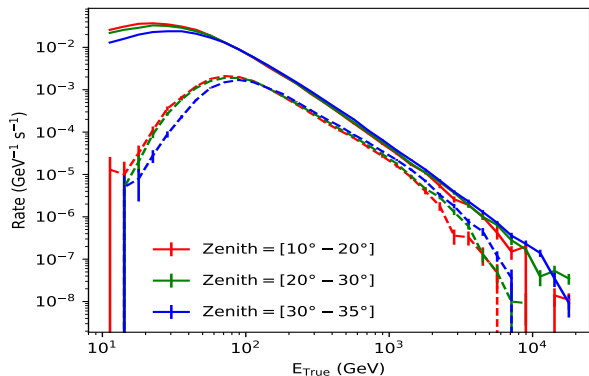


Figure 8: Energy threshold of MACE: The differential γ -ray rate as a function of the true energy. Dashed line curves show γ -ray differential rate after applying the analysis cuts in the zenith angle range 10° - 20° , 20° - 30° and 30° - 35° , while solid lines show rate curves for triggered events in the same zenith angle ranges. The energy threshold shifts from ~ 30 GeV to ~ 80 GeV after applying the analysis cuts.

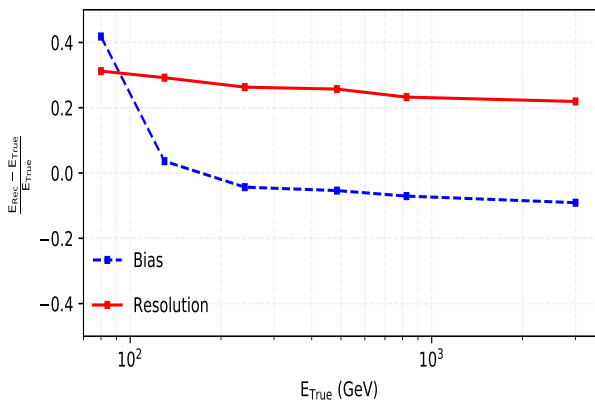


Figure 9: Energy resolution (solid line) and bias (dashed line) of MACE as a function of the true energy of Monte Carlo averaged over zenith angle range of 10° - 35° .

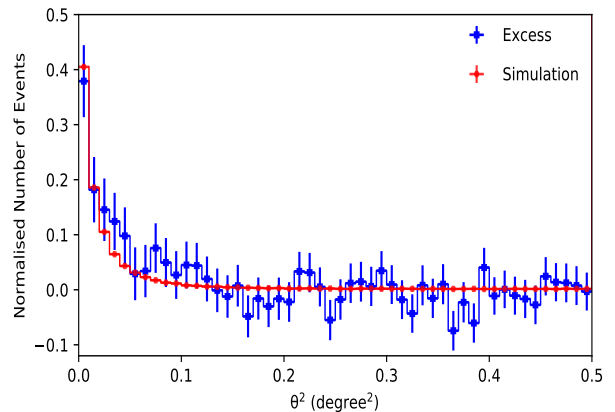


Figure 10: Comparison of background subtracted θ^2 distributions for Crab nebula observations (blue line, filled square) and MC γ -ray events (red, filled circles).

resolution is defined as the standard deviation of the 1-D Gaussian distribution fitted to the distribution of the relative fractional difference between the true and estimated energy. It is expressed as a function of γ -ray energy, $(\frac{E_{est} - E_{true}}{E_{true}} = \frac{\delta E}{E_{true}})$. To estimate the energy resolution, the true γ -ray energies are divided into energy bins. In each bin, the fractional energy $\frac{\delta E}{E_{true}}$ is calculated and fitted with a Gaussian function. The energy bias is defined as the mean of the distribution of fractional deviation of reconstructed energy relative to true energy. Figure 9 shows the variation of the energy resolution (solid red curve) and energy bias (dashed blue line) as a function of true energy of γ -ray events. The energy resolution is determined to be $\sim 34\%$ at the energy threshold (~ 80 GeV), which improves to $\sim 21\%$ above 1 TeV. The energy bias in the corresponding energy range changes from $\sim 42\%$ to $\sim -5\%$.

6.3. Point Spread Function (PSF)

The γ -ray PSF refers to the distribution or spread of reconstructed directions of γ -ray events from a point-like γ -ray source, as detected by the telescope. This distribution peaks at the true source direction, and the spread around the mean value arises due to statistical fluctuations and instrument effects. The error in the reconstruction of the source position is determined by the square of the angular distance between the nominal source position and the reconstructed source position in camera plane, denoted by θ^2 .

We evaluate the PSF of MACE for point-like sources by estimating 68% containment radius for the distribution of

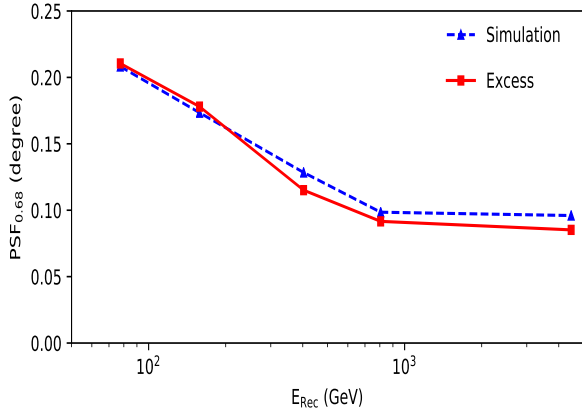


Figure 11: The γ -ray PSF as a function of reconstructed energy from observations (solid line) and simulations (dashed line). It represents the 68% containment radius for the distribution of reconstructed arrival directions around the nominal source location in camera plane.

reconstructed positions around the nominal source location in camera. In case of observations the said quantity can be obtained by calculating the 68 percentile value of the θ^2 distribution of excess events. Figure 10 shows the distribution of θ^2 in excess events obtained from Crab nebula observations. The excess events are calculated by subtracting the θ^2 distribution during OFF runs from θ^2 distribution obtained during ON run. The same figure shows the distribution of θ^2 for simulated γ -ray events. The hadron score cut of $h \leq 0.14$ is applied in addition to quality cuts when finding the θ^2 distributions of data excess as well as simulations. The figure shows a good agreement between the simulated and observed extension of point source.

Figure 11 shows the variation of γ -ray PSF as a function of reconstructed energy γ -ray events, obtained from data and simulations respectively. The two values are consistent with each other, with PSF improving from 0.20° near energy threshold to 0.08° above energy of 1 TeV.

6.4. Integral flux sensitivity

The Integral sensitivity determines the minimum time required for significant detection of a γ -ray source. The minimum integral photon flux emitted by a Crab Nebula like source detectable above a certain energy threshold by an IACT with a 5σ significance in 50 hours of observation, is known as the *Integral flux Sensitivity* of a telescope, subject to the condition that the minimum number of excess γ -ray like events must be at least 10 ($N_{excess} > 10$), and

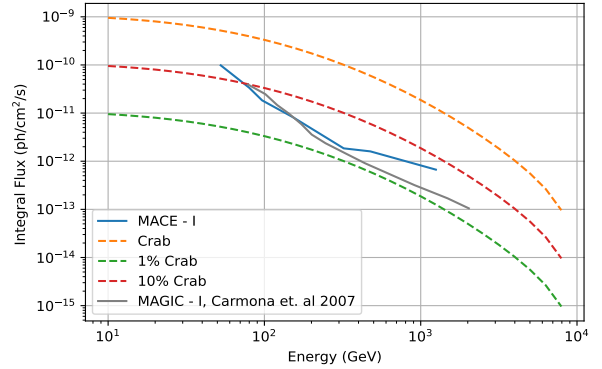


Figure 12: The Integral Sensitivity (the integrated flux of a source above given energy) of MACE, assuming log-parabola spectral shape as a function of true γ -ray energy in the zenith angle range $10^\circ - 35^\circ$, subject to a condition that the minimum number of excess γ -ray like events $N_{excess} > 10$, and ($N_{excess} > 0.05N_{bkg}$). The fractions of the integral Crab Nebula flux are also plotted (1% and 10%) along with the integral flux from MAGIC-I [52] is also shown.

($N_{excess} > 0.05N_{bkg}$). Mathematically, the telescope sensitivity is defined as the flux of a source with $N_{excess} / \sqrt{N_{bkg}} = 5$ after 50 hours of effective observation time. The estimated integral sensitivity of MACE for a Crab Nebula-like source in the zenith angle range $10^\circ - 35^\circ$ above a given energy threshold (E_{th}) is given in Figure 12. Additionally, the integral sensitivity of MACE is compared with that of MAGIC-I telescope [52] along with energy-dependent 1% and 10% Crab Nebula flux. MACE achieves the best sensitivity of $\sim 1.75\%$ of the Crab Nebula flux at ~ 320 GeV. The integral sensitivity of MACE near its energy threshold ($E_\gamma \sim 80$ GeV) is estimated to be $\sim 3.46\%$ of the Crab Nebula flux. It is to be noted that the sensitivity is obtained from ON-observation time only. The quoted MACE and MAGIC-I sensitivity is estimated assuming power law spectral shape for Crab nebula as reported in [52]. On the other hand, the integral flux curves shown for various fractions of Crab flux are calculated with log-parabola spectral shape as reported in [53]. It is evident from Figure 12 that MACE sensitivity is $\sim 10.0\%$ if we assume log-parabola spectral shape for Crab nebula.

7. Results and conclusion

In this section, we present the results obtained by the data analysis of Crab Nebula observations using MACE telescope and calculated the light curve, spectral energy distribution and the flux sensitivity.

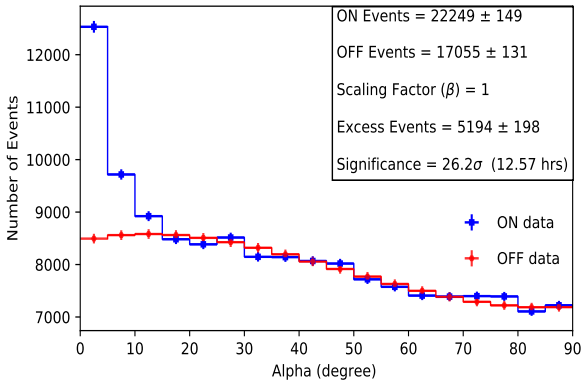


Figure 13: Distribution of the image orientation parameter α for γ -ray events (blue: ON data; red: OFF data) as predicted using the RFM. The γ -ray signal is extracted from the α bin of 10° whereas the background region is considered within $25^\circ \leq \alpha \leq 85^\circ$. The OFF data is normalized between 25 and 85 degrees alpha with respect to the ON data. Subsequently, the ON - OFF information from each bin is utilized to determine the signal.

7.1. Experimental flux sensitivity

For a single imaging Cherenkov telescope, source dependent analysis based on the nominal source position in the camera is more sensitive. Since the IACTs operate in the source tracking mode, the orientation parameter α is very small for the excess γ -ray events, indicating that most of the γ -ray events arrive from the same direction. Consequently, this parameter plays a crucial role in signal extraction. The γ -ray-like events are selected using the α after γ -hadron classification. Figure 13 displays the distribution of events as a function of this parameter after application of gamma-domain and quality cuts. We note that, the average gamma acceptance for the gamma-domain cuts is estimated to be 41.2% while proton rejection is found to be 99.03%. The signal is extracted from the α bin of 10° whereas the background region is considered within $25^\circ \leq \alpha \leq 85^\circ$. We have detected an excess of 5194 ± 198 γ -ray-like events with a statistical significance of 26.2σ in 12.57 hours. These values of significance and time of observation translate to an integral sensitivity of $\sim 9.6\%$ which are consistent with value projected by simulations.

7.2. Differential Energy Spectrum of Crab Nebula

The obtained light curve and the differential energy spectrum are the two important metrics to establish the proper functioning of the telescope. The performance of MACE was further evaluated by estimating the differential energy spectrum. Two factors must be taken into account

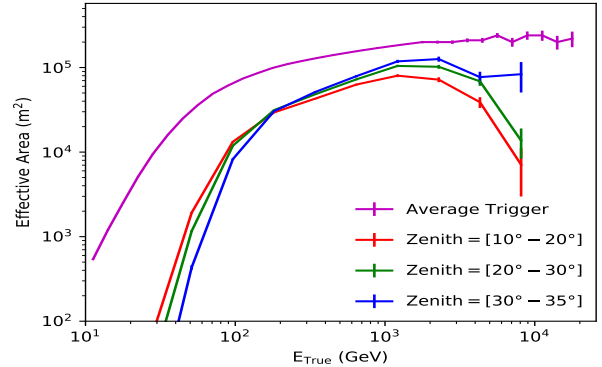


Figure 14: The effective collection area of MACE at the trigger level (magenta color) and after applying the analysis cuts (red, green, blue color) for the zenith angle range $10^\circ - 20^\circ$, $20^\circ - 30^\circ$, $30^\circ - 35^\circ$ respectively.

while determining the differential energy spectrum of the VHE gamma-rays from their observed energy distribution, namely, the finite resolution and finite bias of the energy reconstruction process in imaging Cherenkov telescopes. These factors cause the ‘migration’ of VHE gamma-ray events from their true energy bins to the reconstructed energy bins. The migration of events from true energy bins to nearby reconstructed energy bins is higher at low energies, while it decreases with increasing energy. These effects result in observation of distorted frequency distribution in reconstructed energy as compared to their true energy frequency distribution. The number of observed gamma ray events in reconstructed energy bins are given by

$$Y(E_i) = \sum_{j=1, k=1}^{j=n_a, k=N} A_j^k(E_j) M_{ij}^k(E_j, E_i) S(E_j) \quad (1)$$

Where, $Y(E_i)$ are the total observed events in i th reconstructed energy bin, $A_j^k(E_j)$ is the effective area of the telescope for j th true energy bin during the k^{th} spell of observation, $M_{ij}^k(E_j, E_i)$ represents the element of migration matrix for k^{th} spell, which gives probability that an event in i th bin of reconstructed energy came from j^{th} bin of true energy, $S(E_j)$ are the number of events in the j^{th} bin of true energy, n_a is number of bins in true energy, and N is the total number of observation spells into which data is divided. We have used the method of forward unfolding [54], to estimate differential spectrum of gamma-rays from the observed spectrum in reconstructed energy. The method uses the parametric form $S(E_j; \hat{q})$ for source spectrum where q represents a set of parameters of a spectral

shape to be fitted. A χ^2 statistic is then minimized to find the best fit values of parameters \hat{q} , where χ^2 is given by,

$$\chi^2 = \sum_{i=1}^{i=n_b} \frac{(O(E_i) - \hat{Y}(E_i))^2}{\sigma_i^2} \quad (2)$$

Where, $O(E_i)$ is the observed number of events in i^{th} bin of reconstructed energy, $\hat{Y}(E_i)$ is the estimated counts in i^{th} bin of reconstructed energy based on equation 1 and σ_i^2 are errors in observed events in i^{th} bin of reconstructed energy. The effective area and migration matrices required for the forward unfolding of MACE telescope data were estimated from the γ -ray simulation datasets. We di-

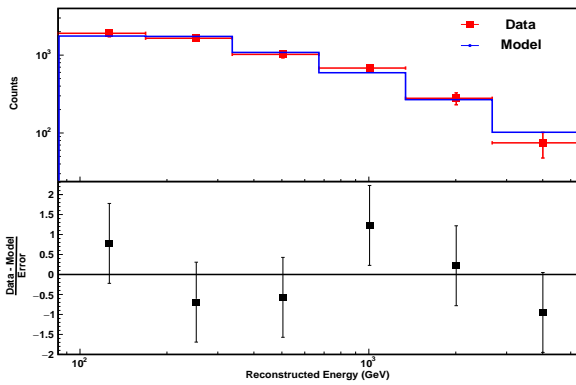


Figure 15: Comparison of observed γ -ray excess counts with γ -ray counts estimated based on forward folded [54] log-parabola spectral model in different bins of reconstructed energy.

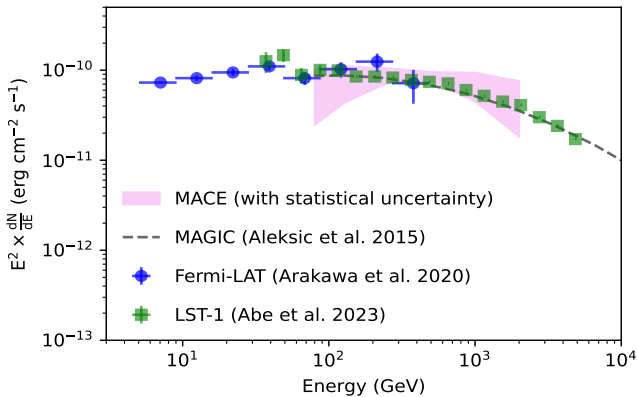


Figure 16: The Spectral energy distribution of the Crab Nebula obtained by MACE (pink shaded region) and its comparison with that obtained by the Fermi-LAT, MAGIC, and LST prototype [48].

vide the dataset into 3 zenith bin ranges of 10-20, 20-30 and 30-35 degrees respectively. Figure 14 shows the effective area in these 3 zenith ranges as a function of energy,

while average migration of events from true energy bins to reconstructed energy bins is depicted in Figure 3.

We use the log-parabola model of differential spectrum, defined as

$$\frac{dN}{dE} = F_0(E/E_0)^{(-\alpha - \beta \log_{10}(E/E_0))} \quad (3)$$

to describe MACE observed energy distribution and compare it with spectrum reported by other groups. The value of E_0 is chosen to be 400 GeV, the energy at which the correlation between the flux normalization and spectral index is minimum. We fit the observed count spectrum in the reconstructed energy range of $80 \text{ GeV} < E_{est} < 5 \text{ TeV}$. The best fit values for the parameters are: $F_0 = (3.46 \pm 0.26) \times 10^{-10} \text{ TeV}^{-1} \text{ sec}^{-1} \text{ cm}^{-2}$; $\alpha = 2.09 \pm 0.06$ and $\beta = 0.08 \pm 0.07$ with χ^2 value of 4.2 for 3 degrees of freedom. Figure 15 shows the comparison between observed excess and estimated γ -ray counts in different bins of reconstructed energy values. The differential flux spectrum of Crab nebula obtained by MACE telescope shows reasonable agreement with measurements reported by other groups. The spectral slope measured by MACE telescope is little harder compared to the slope reported in literature [55], however these values are still within the systematic and statistical errors of each other. It should also be noted that, the systematic uncertainties in MACE observations remain to be estimated.

The spectrum of the Crab Nebula is also presented in the form of Spectral Energy Distribution (SED) and compared with the SED obtained by different telescopes operating in the GeV -TeV energy range, shown in Figure 16. We find that the SED as measured by MACE is in reasonable agreement with SED measurements of other telescopes. We mark that, high error in the curvature parameter of the spectrum reflects in large error bars, specially at TeV energies.

7.3. Lightcurve

The stability of the VHE γ -ray flux from the Crab Nebula over the time scales of days and months was assessed by estimating the light curve of the Crab Nebula above 60 GeV, from MACE observation. Figure 17 displays the light curve showing the daily flux measurements of Crab Nebula from November 15, 2022, to February 23, 2023. The light curve demonstrates the remarkable stability over both days, and months, suggesting that the emission from Crab Nebula remains relatively constant throughout the observation. The small statistical fluctuations indicate the

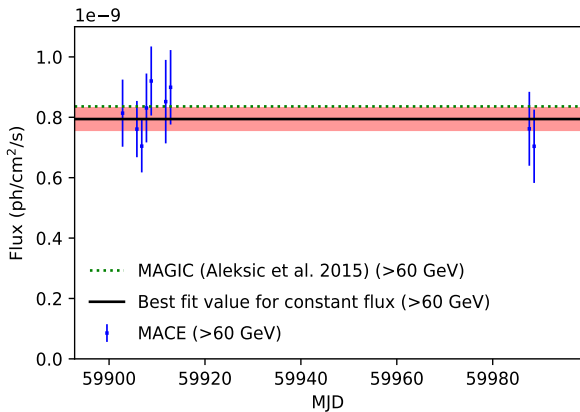


Figure 17: Daily light curve and the statistical error band in the measured mean γ -ray flux of the Crab Nebula for energies above 60 GeV.

accuracy of measurements from MACE. To compare the daily fluxes of Crab Nebula using MACE and the MAGIC telescope, we estimated the integral flux from the MAGIC [10] above 60 GeV, modelled by the log-parabola function and using the best fit parameters. We obtained an integral flux of $(8.35 \times 10^{-10} \text{ ph cm}^{-2}\text{s}^{-1})$ from the MAGIC telescope compared to a flux of $(7.92 \pm 0.36) \times 10^{-10} \text{ ph cm}^{-2}\text{s}^{-1}$ as measured by MACE.

7.4. Conclusion

In this work, we report the results from Crab Nebula observations by the newly commissioned state-of-the-art IACT MACE at Hanle, Ladakh, India. We carried out an extensive MC simulations using the standard CORSIKA package to model the optical and electronics response of MACE telescope. All the analyses were performed using the in-house developed MACE data Analysis Package (MAP). We carried out a comparison of the Hillas parameters of the observed data against those of MC simulations and found them to be in close agreement. We have also investigated intra-night flux variability and found that the emission from the source remained stable, as anticipated. The integral flux sensitivity of the telescope is $\sim 9.6\%$ C.U. above 80 GeV over 50 hours of observations. The best integral sensitivity is achieved for $E_\gamma \geq 320 \text{ GeV}$, which corresponds to $\sim 1.75\%$ of the Crab Nebula flux. The differential energy spectrum from the Crab Nebula measured by MACE in the energy range 80 GeV to 5 TeV is accurately described by a log-parabola function. The spectrum aligns well with the spectrum obtained by the MAGIC telescope within the bounds of systematic and

statistical uncertainties. The SED obtained using MACE telescope is in good agreement with the previous measurements like MAGIC, LST-1 of CTA and Fermi-LAT. An improved analysis method that incorporates the arrival timing of the images will enhance our current estimates. We anticipate an improvement towards the lower energy end of the spectrum following a dedicated low-energy analysis, which will be reported in a subsequent publication. Furthermore, we would like to highlight that since commissioning, all the technical components of the MACE have performed as expected.

References

- [1] V. Trimble, *PASP* 85 (1973) 579.
- [2] K. Lundmark, *Pub. Astro. Soc. Pac.* 33 (1921) 225.
- [3] F. Stephenson and D. GreenBook Review: Historical supernovae and their remnants / Oxford University Press, 2002 Vol. 31 (, 2003).
- [4] T. Velusamy, *Nature* 308 (1984) 251.
- [5] J.R. Graham, G.S. Wright and A.J. Longmore, *ApJ* 352 (1990) 172.
- [6] I.S. Shklovsky, *Radio astronomy*, edited by H.C. van de Hulst Vol. 4, p. 201, 1957.
- [7] X. Sarazin et al., *Astroparticle Physics* 4 (1996) 227.
- [8] R. Novick et al., *ApJL* 174 (1972) L1.
- [9] M. de Naurois et al., *ApJ* 566 (2002) 343, astro-ph/0107301.
- [10] J. Aleksic et al., *Journal of High Energy Astrophysics* 5 (2015) 30, 1406.6892.
- [11] A.K. Tickoo et al., *Pramana* 82 (2014) 585.
- [12] F. Aharonian et al., *ApJ* 614 (2004) 897, astro-ph/0407118.
- [13] S. Lombardi et al., *Astronomy & Astrophysics* 634 (2020) A22, 1909.12149.
- [14] V.A. Acciari et al., *Astronomy Astrophysics* 635 (2020) A158, 2001.09566.
- [15] K. Davidson and R.A. Fesen, *Ann. Rev. Astronomy Astrophysics* 23 (1985) 119.
- [16] J.J. Hester, *Annual Review of Astronomy and Astrophysics* 46 (2008) 127, <https://doi.org/10.1146/annurev.astro.45.051806.110608>.
- [17] A.M. Atayan and F.A. Aharonian, *Monthly Notices of the Royal Astronomical Society* 278 (1996) 525, <https://academic.oup.com/mnras/article-pdf/278/2/525/2793455/278-2-525.pdf>.
- [18] M. Meyer, D. Horns and H.S. Zechlin, *A. & A.* 523 (2010) A2, 1008.4524.
- [19] A.U. Abeysekara et al., *ApJ* 881 (2019) 134, 1905.12518.
- [20] R. Bühler and R. Blandford, *Reports on Progress in Physics* 77 (2014) 066901, 1309.7046.
- [21] A.A. Abdo et al., *Science* 331 (2011) 739, 1011.3855.
- [22] M. Tavani et al., *Science* 331 (2011) 736, 1101.2311.
- [23] R. Buehler et al., *ApJ* 749 (2012) 26, 1112.1979.
- [24] M. Mayer et al., *ApJL* 775 (2013) L37, 1308.6698.
- [25] E. Striani et al., *ApJ* 765 (2013) 52, 1302.4342.
- [26] M. Arakawa et al., *ApJ* 897 (2020) 33, 2005.07958.
- [27] E. Aliu et al., *ApJL* 781 (2014) L11, 1309.5949.

- [28] A. Abramowski et al., *Astronomy & Astrophysics* 562 (2014) L4, 1311.3187.
- [29] F. Aharonian et al., *Chinese Physics C* 45 (2021) 085002.
- [30] T.C. Weekes et al., *ApJ* 342 (1989) 379.
- [31] J. Sitarek, *Galaxies* 10 (2022).
- [32] U.B. de Almeida and M. Doro, *Universe* 8 (2022).
- [33] K.K. Singh and K.K. Yadav, *Universe* 7 (2021).
- [34] R.A. Ong, *Physics Report* 305 (1998) 93.
- [35] C. Borwankar et al., *Astroparticle Physics* 84 (2016) 97.
- [36] M. Sharma et al., *Nuclear Instruments and Methods in Physics Research A* 851 (2017) 125, 1701.01120.
- [37] C. Borwankar et al., *Nuclear Instruments and Methods in Physics Research A* 953 (2020) 163182.
- [38] V.K. Dhar et al., *Journal of Astrophysics and Astronomy* 43 (2022) 17.
- [39] S. Srivastava et al., *Astronomy and Computing* 30 (2020) 100358.
- [40] D. Heck et al., *CORSIKA: a Monte Carlo code to simulate extensive air showers.* (, 1998).
- [41] K. Bernlöhner, *Astroparticle Physics* 30 (2008) 149, 0808.2253.
- [42] C. Borwankar et al., *Astroparticle Physics* 84 (2016) 97.
- [43] C. Borwankar, *MACE Telescope Simulation Software Manual* (, 2019).
- [44] C.S. Stalin et al., *Bulletin of the Astronomical Society of India* 36 (2008) 111.
- [45] S. Ritt, R. Dinapoli and U. Hartmann, *Nuclear Instruments & Methods in Physics Research Section A-accelerators Spectrometers Detectors and Associated Equipment* 623 (2010) 486.
- [46] . HEGRA Collaboration et al., *Astroparticle Physics* 4 (1996) 199.
- [47] A.M. Hillas, *International Cosmic Ray Conference*, edited by . F. C. Jones, , *International Cosmic Ray Conference Vol. 3*, pp. 445–448, 1985.
- [48] H. Abe et al., *ApJ* 956 (2023) 80, 2306.12960.
- [49] L. Breiman, *Machine Learning* 45 (2001) 5.
- [50] F. Pedregosa et al., *Journal of Machine Learning Research* 12 (2011) 2825.
- [51] A. Liaw and M. Wiener, *R News* 2 (2002) 18.
- [52] E. Carmona et al., *International Cosmic Ray Conference*, , *International Cosmic Ray Conference Vol. 3*, pp. 1373–1376, 2008, 0709.2959.
- [53] J. Albert et al., *ApJ* 674 (2008) 1037, 0705.3244.
- [54] J. Albert et al., *Nuclear Instruments and Methods in Physics Research A* 583 (2007) 494, 0707.2453.
- [55] J. Aleksić et al., *Astroparticle Physics* 35 (2012) 435, 1108.1477.

Acknowledgements

The authors sincerely express their profound gratitude to Dr. A. K. Mohanty, Chairman, Atomic Energy Commission, and Secretary, Department of Atomic Energy (DAE), for his deep involvement, continuous support and encouragement during the commissioning phase of the MACE telescope. We are grateful to Shri Vivek Bhasin, Director, Bhabha Atomic Research Centre (BARC) for his inspiring supervision and support in running the observatory at

Hanle. We gratefully acknowledge the valuable guidance, time and efforts provided by Dr. S. M. Yusuf, Director, Physics Group/BARC throughout the successful commissioning and smooth operation of the telescope. We would like to acknowledge the unparalleled contributions made by our colleagues from the Electronics Division, Control and Instrumentation Division, Center for Design and Manufacture, and Computer Division at BARC through their involvements in the indigenous development of the various subsystems of MACE. We thank Dr. Stefan Ritt, Paul Scherrer Institute, Switzerland for technical support in the utilization of Domino Ring Sampler chips in the MACE data acquisition system. We extend our sincere gratitude to the two anonymous reviewers for their critical and insightful comments and suggestions which have undeniably played a pivotal role in the overall improvement of the manuscript.

Data Availability

As an established norms of the field of ground based γ -ray astronomy, regrettably, as of now, the raw data and calibration files generated during various stages of MACE experiment are presently unavailable for external access. The integrity of our research has been maintained by safeguarding all the technical records meticulously.